Rayleigh-Bénard convection with an inclined upper boundary

A. Namiki[*] and K. Kurita[†]

Department of Earth and Planetary Sciences, University of Tokyo, 7-3-1, Hongo, Bunkyo, Tokyo, Japan
(Received 4 September 2001; published 30 April 2002)

We report experiments on thermally driven convection of a high-Prandtl-number fluid with an inclined upper boundary. For an inclined angle greater than the critical value, we observed a few new convection patterns, in which laterally migrating convection cells and plumes appear simultaneously and a large-scale flow is induced from the inclined upper boundary. The plumes induced from the inclined upper boundary activate the temperature fluctuations, resulting in the formation of a large-scale horizontal heat transfer with a lateral scale larger than that of each convection cell. The critical angle for the onset of the lateral migration of the cells is determined by comparing the two length scales: the height difference in one convection cell imposed by the inclined upper boundary and the thickness of the viscous boundary layer.

I. INTRODUCTION

Rayleigh-Bénard convection (RBC), where a horizontal fluid layer is heated from below, is universally found in nature and has been the focus of much research [1,2]. However, most studies of RBC, in experiments and theories, have adopted ideal conditions such as a homogeneous boundary condition and a uniform height of the convection layer. In natural situations, such idealized cases are rare. Recently, there have been several studies devoted to understanding how inhomogeneity affects convection. For example, when both the upper and lower boundaries were inclined, several new types of instabilities and convection patterns were found to exist [3–5]. The rough boundaries modify the plume generation [6], enhance heat transfer [7,8], and modify the statistics of temperature fluctuations [9]. It has also been shown that an inclined bottom boundary enhances heat transfer in a laminar natural convection [10]. These studies show that externally forced boundary conditions critically control the convection, in stark contrast with studies conducted under idealized conditions. Such interactions between externally forced boundary conditions and convection have important clues for understanding the dynamics of RBC.

The problem of how the convecting pattern is determined and how the heat transfer is modified when the Rayleigh number varies in a single convecting layer is an important issue. A simple case suitable for studying such a problem is that of an RBC in which the upper boundary is inclined. We used a high-Prandtl-number fluid because the convective states change when the Rayleigh number is varied over the wide range used in our experiments [11–13]. When the upper boundary is inclined, the Rayleigh number varies laterally. As a result, different convecting patterns adjacent to each other interact to produce a new pattern. This also strongly modifies the heat transfer. Such a situation actually exists in the interiors of the Earth, planets, and stars and is an important engineering problem. In the present study, we conducted experiments to investigate how the inclined upper boundary of the convection layer affects the RBC.

II. EXPERIMENTAL SETTINGS

A. Experimental apparatus

We conducted thermal convection experiments with an inclined upper boundary and observed the temperature fields using a thermotropic liquid crystal powder, which changes the reflective color within the prescribed temperature range. The experimental apparatus used in this work is shown in Fig. 1. The fluid tank in these experiments is rectangular in shape (500 mm in length and 50 mm in width). We adopted this narrow width to obtain a clear temperature field. The inclined angle is varied by independently changing the height of both sides of the lid. The side walls are made of acrylic plates with a thickness of 15 mm. The upper and lower boundaries are made of aluminum and copper plates with a thickness of 3 mm and 2 mm, respectively. The tank is filled with glycerol solution, which is heated from below and cooled from above. The temperature of the upper and lower boundaries is controlled by circulating water at a precision of $\leqslant 0.1\,°C$. Three small movable thermistor probes (3.2 mm in length and 0.35 mm in diameter) are placed inside the cell in
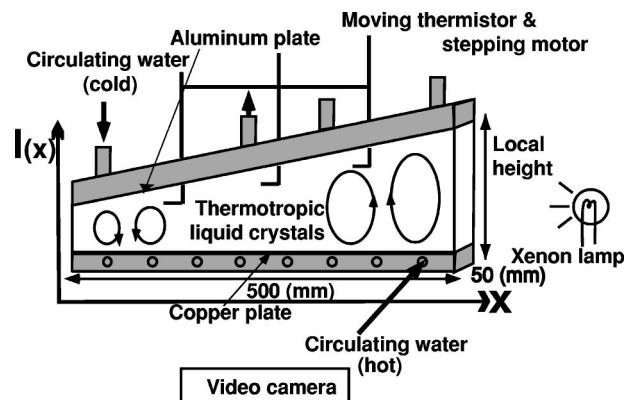

FIG. 1. A sketch of the experimental apparatus.

*Present address: Department of Earth Sciences, Kanazawa University, Kakuma-machi, Kanazawa 920-1192, Japan. Electronic address: namiki@earth.s.kanazawa-u.ac.jp

†Present address: Earthquake Research Institute, 1-1-1 Yayoi, Bunkyo-ku, Tokyo 113-0032, Japan.

order to measure the vertical temperature profile of the convecting fluid. The probes are mounted on a stepping motor so that the local temperature of the fluid can be measured as a function of the distance away from the upper and lower boundary with an accuracy of 0.01 mm. Each movable thermistor is calibrated with an accuracy of 0.01 °C.

The Rayleigh number is varied by changing the local height of the convection layer [$8 < l(x) < 140$ mm], the temperature difference between the upper and lower boundaries ($4 < \Delta T < 19$ °C), and the concentration of glycerol (i.e., kinematic viscosity, $3 \times 10^{-5} < \nu < 5 \times 10^{-4}$ m²/s). The maximum inclined angle is 14°. The viscosity of glycerol is only weakly temperature dependent, and its variation is less than a factor of 5 in a single experiment. The Prandtl number ($240 < \mathrm{Pr} = \nu/\kappa < 4200$) is also varied by the concentration of glycerol, where κ is the thermal diffusivity.

B. An estimate of several scales of flow

Before describing the experimental results, we show some scalings that predict the characteristics of the convection under the inclined upper boundary. We derived some scalings based on the scalings for the leveled upper boundary cases.

In our experimental situation, under the inclined upper boundary, the Rayleigh number varies laterally because of the thickness variation, $l(x)$. The direction of x is denoted in Fig. 1. We define the local Rayleigh number as

$$\mathrm{Ra}_l(x) = \frac{\alpha g \Delta T l(x)^3}{\nu \kappa} \tag{1}$$

$$= \mathrm{Ra}_c \left[\frac{l(x)}{l_c} \right]^3, \tag{2}$$

where α is the thermal expansion coefficient, g is the gravitational acceleration, $\mathrm{Ra}_c \sim 10^3$ is the critical Rayleigh number [14,1], and l_c is the thickness of the convection layer at $\mathrm{Ra}_l(x) \sim \mathrm{Ra}_c$. This equation shows that $\mathrm{Ra}_l(x)$ is only a function of $l(x)$ in a single experiment.

1. The thickness of the thermal boundary layer

The thickness of the thermal boundary layer, δ_{th}, is estimated as follows. The thickness of the thermal boundary layer has been determined experimentally in the case with a leveled upper boundary as

$$\delta_{th}(x) \sim \frac{l(x)}{2\,\mathrm{Nu}} \sim \frac{l(x)}{2\,\gamma [\mathrm{Ra}_l(x)/\mathrm{Ra}_c]^\beta}, \tag{3}$$

where Nu is the Nusselt number and γ is an experimentally determined constant. Since convection in the experiments is not in the regime of fully developed turbulence and $\mathrm{Pr} \gg 1$, it follows that $1 < \gamma < 2$ and $\beta \sim 1/3$ [2,15]. Substituting $\beta \sim 1/3$ and Eq. (2) for Eq. (3) yields

$$\delta_{th}(x) \propto l_c. \tag{4}$$

This indicates that the thickness of the local thermal boundary layer is independent of the local height of the convecting layer.

2. Flow velocity

The scaling laws to estimate the flow velocity under the leveled upper boundary depend on the convection regimes. We estimate the flow velocity in two regimes based on the leveled cases: the regime when convection cells are observed ($\mathrm{Ra} \lesssim 10^6$) and the regime when plumes are dominant ($10^7 < \mathrm{Ra} < 3 \times 10^8$).

When the convection pattern shows convection cells, the convecting velocity is estimated following the simple boundary layer analysis of a finite-amplitude convection with an aspect ratio of 1. The convecting velocity $u(x)$ is written as

$$u(x) \sim \frac{\kappa}{l(x)} \mathrm{Ra}_l(x)^{2/3}. \tag{5}$$

Substituting Eq. (2) for Eq. (5) yields

$$u(x) \sim \frac{\kappa}{l_c^2} \mathrm{Ra}_c^{2/3} l(x). \tag{6}$$

This equation indicates that the convecting velocity is a function of $l(x)$. Since the time scale for the overturn, τ_c, is of the order of $4l(x)/u(x)$,

$$\tau_c \propto l_c^2 \kappa^{-1} \mathrm{Ra}_c^{-2/3}, \tag{7}$$

which shows that the time scale of the overturn does not depend on the local height of the convection layer.

When the convection is dominated by plumes, the convecting velocity depends on the velocity of the plumes. Because of the large Prandtl number, the velocity of the plumes can be estimated by the Stokes velocity,

$$v_{st} \sim \frac{g \alpha \Delta T \delta_{th}^2}{3\nu}. \tag{8}$$

To calculate the Stokes velocity, we use the thickness of the thermal boundary layer as the radius of the plume head. Using Eqs. (2) and (4) yields

$$v(x)_{st} \propto \frac{\kappa}{3 l_c} \mathrm{Ra}_c. \tag{9}$$

This equation indicates that the convecting velocity is independent of $l(x)$.

3. Heat flux

In order to compare the local heat flux at different sites in a single experiment, we introduce a new parameter, q_n:

$$q_n \sim \frac{J[\mathrm{Ra}_l(x)]}{J[\mathrm{Ra}_c]} \sim \frac{k \Delta T / \delta_{th}}{k \Delta T / l_c}, \tag{10}$$

where k is the thermal conductivity and J is the heat flux. Here, we assume that the heat flow is determined by $\mathrm{Ra}_l(x)$,

which implies that the lateral heat transfer is ignored. For $Ra_l(x) > Ra_c$, using Eqs. (4) and (10), q_n becomes

$$q_n \sim \frac{l_c}{\delta_{th}} \sim 1, \tag{11}$$

which shows that q_n is independent of the thickness of the convection layer.

III. RESULTS

A. Pattern observation

Experiments were carried out at $10^3 < Ra_l(x) < 3 \times 10^8$. When the upper boundary is leveled, four regimes are observed: $10^3 < Ra < 10^6$, two-dimensional steady convection cells; $10^6 < Ra < 10^7$, a time-dependent convection; $10^7 < Ra < 10^8$, a plume-dominant convection; and $3 \times 10^8 \leqslant Ra$, a large-scale flow. The convection pattern does not show three-dimensional convection cells for $Ra < 10^6$ because the width of the adopted convection tank is much smaller than its length. Otherwise, the convection pattern is consistent with those of previous studies (e.g., [12,13]).

Figure 2(a) shows snapshots of the temperature field of convection when the inclined angle is $12°$. The time-dependent feature of convection patterns is observed, although the local Rayleigh numbers are in the range of $10^4 < Ra_l(x) < 10^6$ within which the convection pattern is classified into a regime of steady convection cells when the upper boundary is leveled. Convecting cells migrate from the thicker region toward the thinner region, as shown by the green arrows. The migrating velocity at thinner regions is higher than that at thicker regions. Because of this lateral variation of the migrating velocity, the convection cells adjust as follows. In the thick region, each cell elongates laterally and eventually separates into two cells, whereas, in the thin region, the cells coalesce. When the convection cells separate and coalesce, three-dimensional plumes are observed, as indicated by red and yellow circles. Cold plumes migrate from the thicker region toward the thinner region, whereas hot plumes migrate in the opposite direction.

Figure 2(b) shows the time-evolution of the migrating velocity; the variation of the migrating velocity of the cells can be clearly seen. The deep blue and deep yellow regions show the sites of the upwellings and downwellings, respectively. The convection cells at thicker regions (right) migrate toward the thinner region (left). The steepness of the slope angle of the yellow and blue regions indicates the migrating velocity. The migrating velocity for the thinner region is faster than that for the thicker region. However, the slope angle at the thinnest region is zero, which means that there is no migration there. Between the regions of migration and absence of migration, the convection cells show oscillation. This is related to the plumes observed when the convection cells separate and coalesce.

Under a case with a leveled upper boundary, convection cells are observed at a lower Rayleigh number ($Ra < 10^6$). The convection cells stay at the same sites and never migrate systematically in the lateral direction. On the other hand, plumes are observed under a higher Rayleigh number (Ra

$> 10^6$). We note that, for the case with an inclined upper boundary, two convection patterns, i.e., convection cells and plumes, appear simultaneously.

Figure 3(a) shows snapshots of the temperature field of convection when the local Rayleigh numbers are higher than in the case of Fig. 2. Here, the inclined angle is $10°$ and $4 \times 10^6 < Ra_l(x) < 4 \times 10^7$. A large-scale flow of convection patterns is observed, although the local Rayleigh numbers are $Ra_l(x) < 4 \times 10^7$, much lower than the Rayleigh number at which a large-scale flow is observed under the leveled upper boundary ($Ra \geqslant 3 \times 10^8$). The large-scale mean flow consists of cold plumes sliding down the slope and hot plumes being swept in the opposite direction by the counterflow.

Figure 3(b) clearly shows the site of the swept hot plumes. The blue lines from the left to the right indicate the loci of swept hot plumes, which stop at the right end of the tank. Yellow spots at the left end of the tank are the accumulation of cold plumes sliding down the slope. The blue lines are nearly parallel to each other. This indicates that the migrating velocity does not depend on the local height.

Figure 4 summarizes the series of pattern observations and shows the regime for migrating convection cells. This figure shows that (a) there is a critical angle, above which the convection cells migrate toward the thinner region and (b) this critical angle is a function of $Ra_l(x)$. The region where oscillations are observed is in the vicinity of the regime boundary.

B. Temperature measurements

Pattern observations show that the inclined upper boundary causes the convection cells and plumes to migrate horizontally. Furthermore, plumes are observed at $Ra_l(x) < 10^6$, and a large-scale flow is observed at $Ra_l(x) < 4 \times 10^7$. These local Rayleigh numbers are smaller than those under leveled boundaries. These results suggest that the inclined upper boundary increases the effective Rayleigh number. The properties of the temperature fluctuation and its frequency spectrum, histograms, and time derivative have been known to provide important information of the thermal and kinematic energy state of the convection (e.g., [1,16,17]). Accordingly, we studied these properties under the inclined upper boundary.

1. Leveled upper boundary

We describe the characteristics of the temperature fluctuations under the leveled upper boundary at a high Prandtl number before describing the characteristics of those under the inclined upper boundary.

Figure 5(a) shows the temperature-time series data. Dotted and solid lines show the cases of $Ra \sim 10^6$ and 4×10^7, respectively. The convection pattern at $Ra \leqslant 10^6$ under the leveled upper boundary shows steady convection cells. A thermistor probe inserted in the convection layer does not detect the temperature fluctuations because of the steadiness of the convection cells, as shown by the dotted line. On the other hand, at a high Rayleigh number, the solid line shows large fluctuations, which are related to the passing hot and
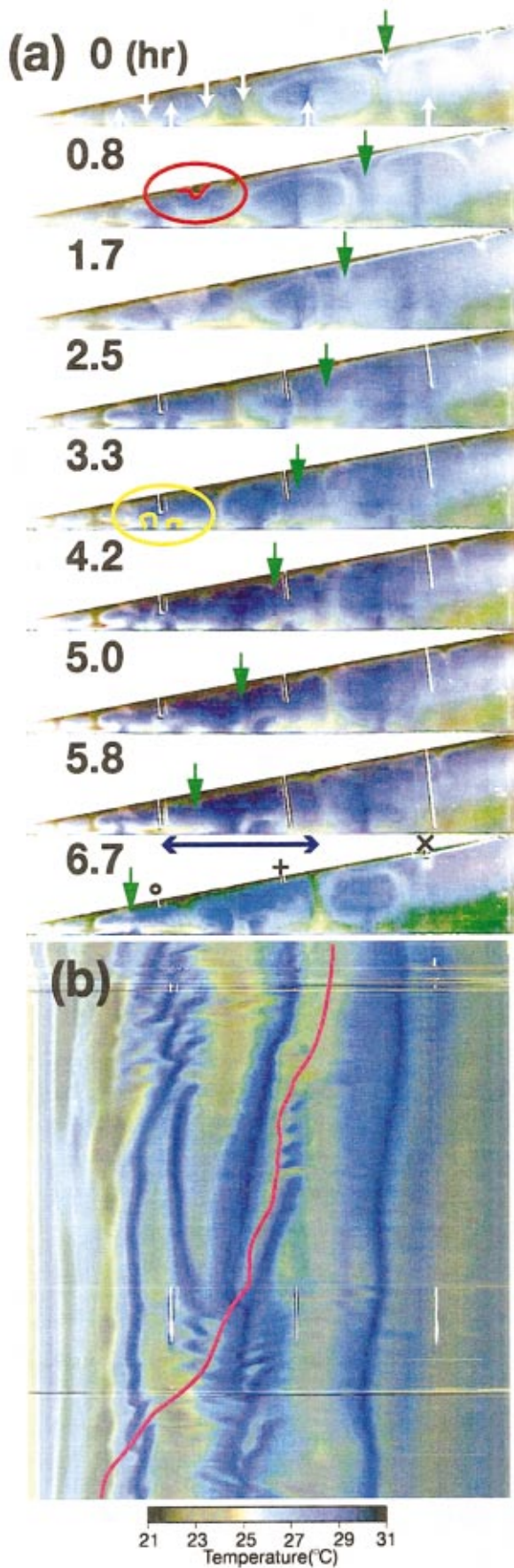
FIG. 2. (Color) (a) A time-series of snapshots of the temperature field. Red/yellow areas correspond to low-temperature regions (downwelling sites in convection cells), and blue ones to high-temperature regions (upwellings). White arrows indicate the upwelling and downwelling sites. Numbers shown in the left indicate the time elapsed after achieving thermal equilibrium. White lines are thermistor probes. Green arrows indicate the site of a downwelling. The yellow circle indicates the coalescence of convection cells. The red circle indicates the separation of convection cells. The blue arrow indicates a pair of laterally elongated convection cells. Experimental conditions are $10^4 < \mathrm{Ra}_l(x) < 10^6$ and $23 < l(x) < 110$ mm, and the inclined angle is $12°$. The horizontal width of each snapshot is 0.5 m. $\bigcirc$, $+$, and $\times$ in the bottom snapshot show the sites of thermistor probes. (b) Temperature profile at the bottom traced through time (time increases toward the bottom) for (a). The time span and horizontal width are the same as in (a). The red line shows the site of the downwelling indicated by the green arrows in (a).
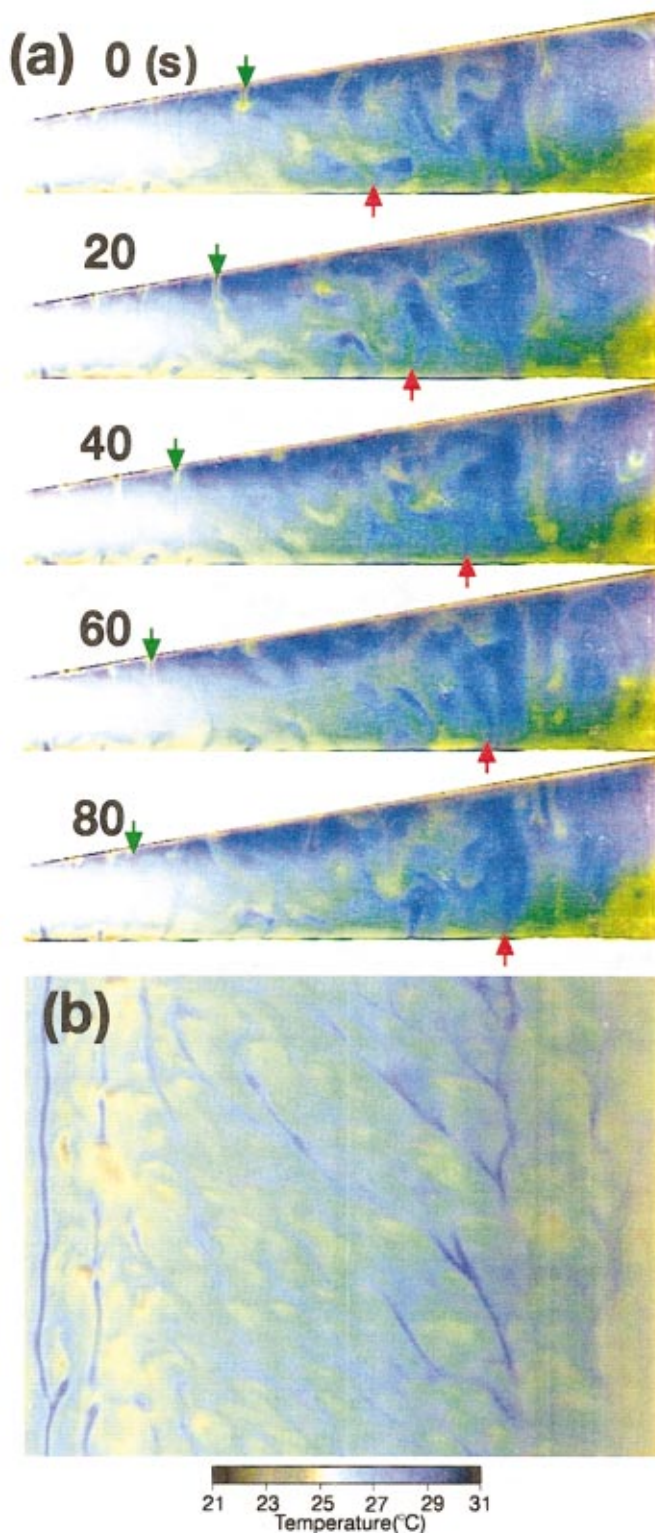
FIG. 3. (Color) (a) Same as Fig. 2, but for $4 \times 10^6 < \mathrm{Ra}_l(x) < 4 \times 10^7$, $104 < l(x) < 140$ mm, and an inclined angle of $10°$. Green and red arrows indicate the site of a cold and hot plume, respectively. (b) Temperature profile at the bottom traced through time for (a). The time span is 7 min.

cold plumes [18]. These characteristics can also be identified from the histogram of the temperature variation [Fig. 5(c)]. The solid line indicates wider distributions than those of the dotted line. The solid line shows a symmetrical distribution, which means that the probability of the occurrence of the passing hot and cold plumes is the same. The deviation of the mean temperature from 0.5 at the middle height is caused by the temperature dependence of the glycerol viscosity (see Appendix).

The dotted line in Fig. 5(b) shows the frequency power spectrum of (a). The power decreases linearly with the frequency, ω. The spectra at $\mathrm{Ra} \lesssim 10^6$ and the thermal diffusion show similar profiles and suggest that they are controlled by thermal diffusion alone and not by convective velocity. On the other hand, when the Rayleigh number is larger than that of the time-dependent regime, the magnitude of the power at lower frequency is increased, and the slope of the frequency power spectrum becomes steeper. The solid line shows the power spectra at $\mathrm{Ra} \sim 4 \times 10^7$, where the convection pattern is plume dominant. It is known that in the fully developed thermal convection, the exponent becomes $\omega^{-1.4}$ [16,19]. However, our measurements show that the frequency range that shows this exponent law is very narrow, indicating that the convection is not fully developed turbulence.

Figure 5(d) shows the histogram of the time derivative of the temperature. The width of the histogram shows the passing velocity of the plumes and upwellings/downwellings compared with the diffusive time scale of the thermal boundary layer. When convection cells are observed, the horizontal migration of cells is negligible or very slow, if at all observed. The narrow width of the dotted line indicates the negligible/slow migration of the convection cells. When plumes are dominant, the width of the histogram indicates the velocity of the plumes. Since plumes are caused by thermal buoyancy in our experiments, temperature fluctuations show asymmetry: a rapid initial increase (decrease) in temperature, followed by a more gradual decrease (increase), as shown in Fig. 5(a) [17]. Thus, hot (cold) plumes skew the histogram toward the positive (negative). The symmetry of the histogram indicates the symmetric passing of the hot and cold plumes.

2. Temperature fluctuations caused by migrating convection cells

Figure 6(a) shows the temperature-time series data. The experimental conditions are $5 \times 10^3 < \mathrm{Ra}_l(x) < 3 \times 10^6$ and $13 < l(x) < 115$ mm, and the inclined angle is $14°$, i.e., the experimental conditions are nearly identical to those in Fig. 2, and the observed convection pattern is similar to that in Fig. 2. Solid, dashed, and dotted lines show the temperature variation at the sites of $\mathrm{Ra}_l(x) \sim 9 \times 10^4, 6 \times 10^5$, and 2×10^6, respectively. The temperature variation is characterized by the large amplitude than that in the case under the leveled upper boundary at $\mathrm{Ra} \sim 10^6$ [Fig. 5(a)]. The mean temperature in the thinnest region is lower than that in other regions.

A large fluctuation and the skewed mean temperature are also evident from the histogram [Fig. 6(c)]. The width of the temperature distributions of Fig. 6(c) is much larger than that under the leveled case [Fig. 5(c)]. The temperature distribu-
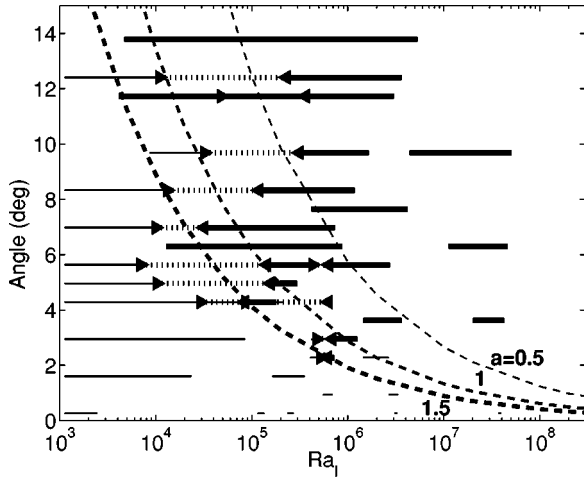
FIG. 4. The regime diagram of convection patterns. Each segment shows the range of a single experiment. Thick lines indicate the ranges of $Ra_l(x)$, where the migration of convection cells is observed, and thin lines indicate those where the convection pattern resembles the leveled case. Dotted lines between the right and left pointed triangles indicate the ranges where the oscillations were observed. Dashed lines indicate the calculated critical angle by Eq. (15) with $a \sim 0.5$, 1, and ~ 1.5 from the thinner line.
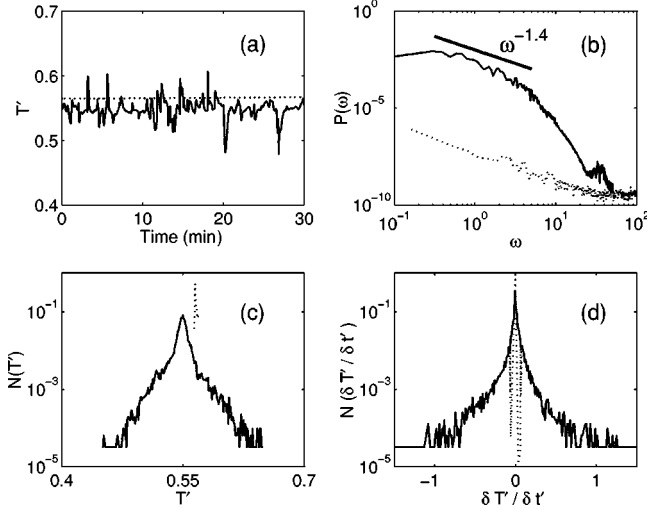

FIG. 5. (a) Time series of the temperature variation T' under the leveled upper boundary, which is measured at the middle height and the center of the convection cell and is normalized by the temperature difference between the upper and lower boundaries, $(T - T_l)/\Delta T$, where T_l is the temperature at the upper boundary. Dotted and solid lines show the case of $Ra \sim 10^6$ and 4×10^7, respectively. (b) Power spectrum for (a). The frequency ω is normalized by the thermal diffusive time of the thermal boundary layer, δ_{th}^2/κ. (c) Measured temperature histogram N as a function of T' for (a). N is scaled by the total number. (d) Histogram of the time derivative of the temperature, N, as a function of $\delta T'/\delta t'$ for (a). The time scale $\delta t'$ is normalized by the thermal diffusive time of the thermal boundary layer, δ_{th}^2/κ.
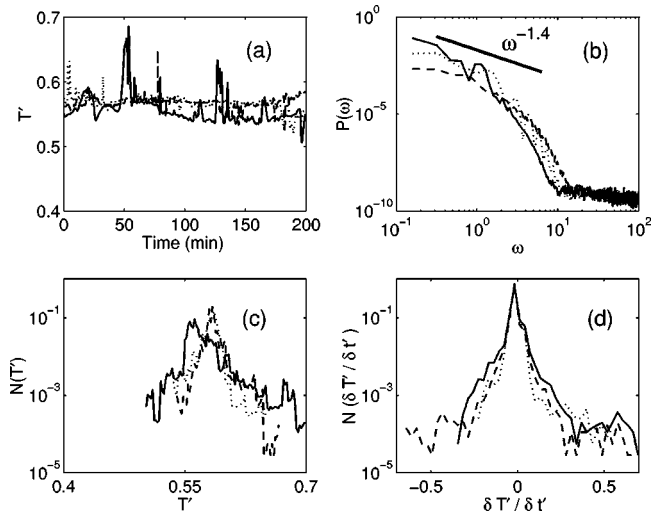

FIG. 6. Same as Fig. 5, but for the case under the inclined upper boundary. Experimental conditions are $5 \times 10^3 < Ra_l(x) < 3 \times 10^6$ and $13 < l(x) < 115$ mm, and the inclined angle is $14°$. Solid, dashed, and dotted lines show the temperature variation at the site of $Ra_l(x) \sim 9 \times 10^4, 6 \times 10^5$, and 2×10^6 from the thinner region, respectively. The horizontal locations of probes are shown in Fig. 2.

tions for the thicker region (dotted and dashed lines) show a symmetric distribution with respect to their mean, while those for the thinner region exhibit an asymmetric distribution with respect to their mean. The mean temperature of the thinner region is lower than that of the thicker region, and the presence of positive spikes of temperature variation causes a positive skewness of distribution. This is the consequence of cold downwellings being pinned at the thin region with the occasional passing of the hot plumes.

Figure 6(d) shows the distribution of the time derivative of the temperature. There are three peaks: the main distribution at the center and small lumps at either side. The main distribution and the lumps might be related to the migration of convection cells and plumes, respectively. The width of the main distribution is larger than that under the leveled upper boundary, which is less than ± 0.1 [Fig. 5(d)]. This suggests that the width of the histogram is related with the migrating velocity of the convection cells originating from the inclined upper boundary. Here, the width of the main distribution is larger for thinner regions (solid line). The large width of the main distribution is related with the rapid migrating velocity and steep temperature gradient caused by the small convection cells. This is consistent with the visual observation [Fig. 2(b)], which shows a faster migrating velocity for the thinner region, and shows the smaller convection cells because of its height.

The power spectrum under the inclined upper boundary also shows distinctive features. For example, the power spectrum under an inclined upper boundary with $5 \times 10^3 < Ra_l(x) < 3 \times 10^6$ [Fig. 6(b)] differs from that under the flat boundary with $Ra \sim 10^6$ [Fig. 5(b), dotted line] and resembles that with $Ra \sim 4 \times 10^7$ [Fig. 5(b), solid line]. Here, the Rayleigh number of the dotted line in Fig. 5(b) is in the range of the local Rayleigh number of Fig. 6(b). We can interpret this similarity to arise from the presence of horizontally migrat-
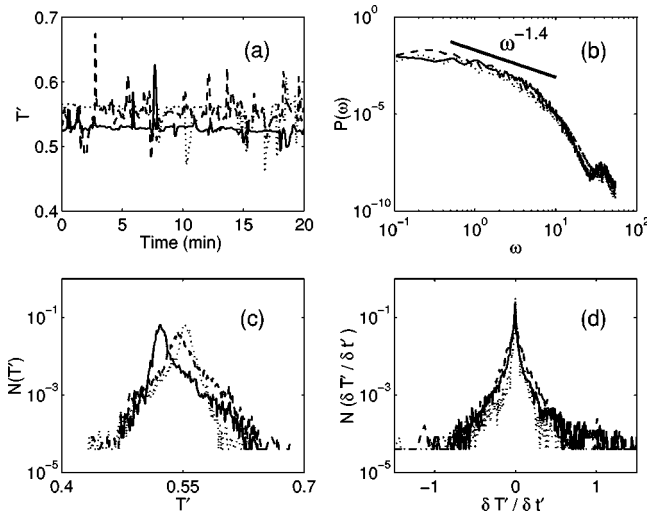
FIG. 7. Same as Fig. 6, but for $4 \times 10^6 < \mathrm{Ra}_l(x) < 4 \times 10^7$, $104 < l(x) < 140$ mm, and an inclined angle of $10°$. The $\mathrm{Ra}_l(x)$ at each site of the probe is 8×10^6, 10^7, and 3×10^7 from the thinner site.

ing convection cells and plumes under the inclined upper boundary.

3. Temperature fluctuations caused by migrating plumes

Figure 7(a) shows the temperature-time series data for Fig. 3. The local Rayleigh numbers of each site are 8×10^6, 10^7, and 3×10^7 from the thinner site. Although the smallest local Rayleigh number of Fig. 7 [$\mathrm{Ra}_l(x) \sim 4 \times 10^6$] and the highest local Rayleigh number of Fig. 6 (3×10^6) are similar, the time scale of the temperature fluctuation of Fig. 7(a) is much less than that for Fig. 6(a). Furthermore, the time scale of the temperature fluctuation of Fig. 7(a) is less than that for Fig. 5(a), where $\mathrm{Ra} \sim 4 \times 10^7$ corresponds to the highest local Rayleigh number of Fig. 7. This characteristic can also be identified from Fig. 7(b). The magnitude of the power at high frequency is larger than that of Figs. 6(b) and 5(b). The differences of the power spectra among the three sites of the probes are negligible in spite of the different local Rayleigh number.

The histogram of the temperature variation [Fig. 7(c)] of the thinner region, shown by the solid line, has a lower mean value and a positive skewness of distribution. We interpret this distribution to be the result of the accumulation of cold plumes with the occasional interference of rising hot plumes. In contrast, the histogram of the temperature variation in the thick region, shown by a dotted line, has a higher mean value. This can be interpreted to be the result of the accumulation of warm plumes in this region.

The time derivative of the temperature exhibits a similar tendency. In the thin region [solid line in Fig. 7(d)], the distribution shows an asymmetry that has a larger deviation for positive values than that for negative values (positive skewness).

We find that the characteristics of the temperature fluctuations in the regime of the new convection pattern are similar to those of the leveled upper boundary at a Rayleigh number
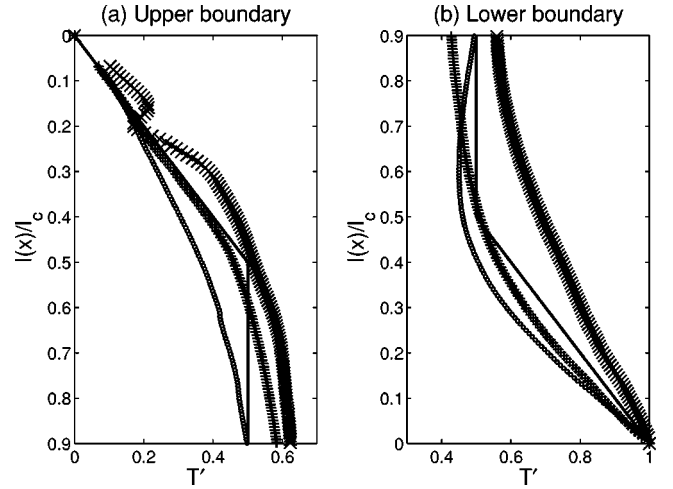

FIG. 8. Vertical temperature profiles of (a) upper and (b) lower boundaries for the case of $4 \times 10^3 < \mathrm{Ra}_l(x) < 4 \times 10^5$. Locations of probes are shown in the bottom snapshot of Fig. 2. $\mathrm{Ra}_l(x)$ values at each site are 2.8×10^4, 1.1×10^5, and 3.2×10^5 from the thinner region. Heights are normalized by the thickness at $\mathrm{Ra}_l(x) \sim \mathrm{Ra}_c$. The bold line is the reference temperature profile for the leveled case. The $\times$ line twists in (a) are caused by a lateral passing of a cold plume.

larger than the highest local Rayleigh number of the inclined case.

C. Temperature profile

We measured the vertical temperature profile at three sites to calculate the heat flux. Figure 8 shows the vertical temperature profiles in a convecting fluid. It shows that the temperature gradient increases (decreases) where the convection layer is thick (thin) for the upper boundary and vice versa for the lower boundary. This diagram shows that the thickness variation of the convecting layer enhances the lateral variation of the heat flux.

IV. DISCUSSION

A. A model for the critical angle

We showed that the inclined upper boundary modulated the convection pattern and its vigor. Figure 4 shows that there is a critical angle that controls the convective regimes and that an oscillation occurs around this critical angle. We estimate the critical angle as follows.

We introduce an assumption in which the critical angle needed for the lateral migration of the convection cells is determined by comparing the two length scales, δ_h and $\delta_v / \cos(\theta)$, as shown in Fig. 9. Here, δ_h is the height difference in one convection cell caused by the inclined upper boundary, δ_v is the thickness of the viscous boundary layer, and θ is the inclined angle of the upper boundary. The shaded area will be cooled from above. If δ_h is smaller than $\delta_v / \cos(\theta)$, a viscous force suppresses the instability in the shaded area. However, if δ_h is larger than $\delta_v / \cos(\theta)$, the shaded area becomes unstable to negative buoyancy. In other words, the convection cells are deformed by the inclined upper boundary up to the length scale δ_v without the migra-
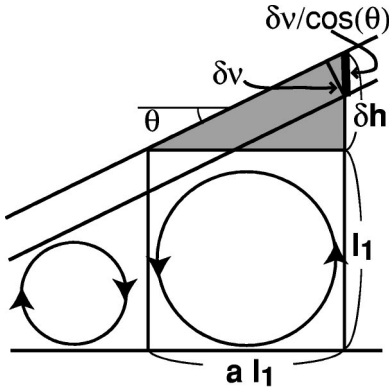
FIG. 9. A cartoon of the convection cells.

tion. When the deformation of the convection cell exceeds the length scale δ_ν, the cell cannot maintain its location or shape and initiates the migration.

Thus, the critical angle is estimated from

$$\delta_h \sim \frac{\delta_\nu}{\cos(\theta_c)}, \tag{12}$$

where θ_c is the critical angle for the migration of convection cells. δ_h is expressed by

$$\delta_h \sim a l_1 \tan(\theta), \tag{13}$$

where a is the aspect ratio of the convection cell and l_1 is the height of the shorter side of the cell. The thickness of the viscous boundary layer can be estimated to be of the same order as the velocity boundary layer, which is of the same order of the thickness of the thermal boundary layer δ_{th} at these Rayleigh numbers [20]. In a strict sense, there is a difference between the thicknesses of the thermal and viscous boundary layers, especially in the fully developed turbulence [20,21]. We use the thickness of the thermal boundary layer as an order estimate of the thickness of the viscous boundary layer. The thickness of the thermal boundary layer is written by Eq. (3). Thus, the thickness of the viscous boundary layer is expressed by

$$\delta_\nu \sim \delta_{th} \sim \frac{1}{2} l_1 \left[\frac{Ra_c}{Ra_l(x)} \right]^{1/3}. \tag{14}$$

Substituting Eqs. (13) and (14) into Eq. (12), we obtain the critical angle as

$$\theta_c \sim \sin^{-1} \left\{ \frac{1}{2a} \left[\frac{Ra_c}{Ra_l(x)} \right]^{1/3} \right\}. \tag{15}$$

In Fig. 4, we draw three curves of calculated critical angles using Eq. (15) for $a=1.5$ (thick line), 1 (medium line), and 0.5 (thin line). The experiments do not show the uniform aspect ratio of convection cells, since the inclined upper boundary elongates the convection cells because of separation and coalescence. The observed maximum and minimum of the aspect ratio of the convection cells are $a \sim 1.5$ and 0.5, respectively. Figure 4 shows that the calculated critical angle is consistent with the experiments.
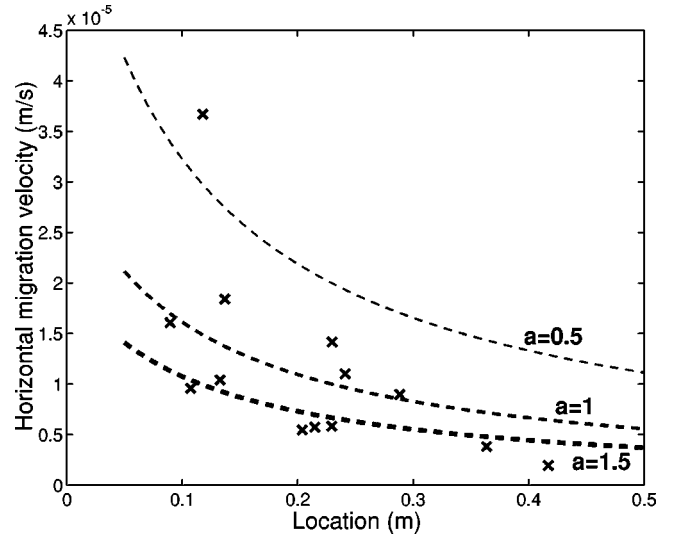

FIG. 10. The velocity of the horizontal migrations of convection cells. $\times$ shows the migrating velocity of convection cells. Dashed lines show the calculated velocity by Eq. (16) with $a \sim 0.5, 1$, and 1.5 from the thinner line.

This scaling also indicates that the critical angle asymptotically approaches 0 as $Ra_l(x)$ increases. What kind of convection pattern would be observed when the critical angle is close to 0? There is a clue in Fig. 3 for us to infer the pattern. The observed convection pattern of Fig. 3 resembles the large-scale flow. In our experiments, the large-scale flow is observed at $Ra > 3 \times 10^8$ under the leveled upper boundary case. The critical angle at $Ra \sim 3 \times 10^8$ is less than $1°$. It is probable that the large-scale flow appears when the critical angle is close to 0 as the Rayleigh number increases.

B. Migrating velocity

Next, we show that the length scale δ_h can also explain the migrating velocity of the convection cells. In our model, the time scale for the instability is determined by the thermal diffusion time of the δ_h. This suggests that the migrating velocity of the convection cells is related to the thermal diffusion velocity κ/δ_h. We compared the thermal diffusion velocity with the migrating velocity of the convection cells based on the case of Fig. 2. The dashed lines in Fig. 10 show the thermal diffusion velocity of

$$v_m \sim \kappa/\delta_h. \tag{16}$$

Here, we computed three cases of $a=1.5$ (thick line), 1 (medium line), and 0.5 (thin line). Figure 10 shows that the general trend and its magnitude estimated from this relation agree well with the measurements. We show the estimation of the circulating velocity of convecting cells in Eq. (6), which increases as a function of the local height of the convecting layer. We note that this dependence is inverse to that of the migration velocity.

When plumes are mainly observed, the migrating velocity is described by a different scaling. Figure 3(b) shows that the migrating velocity of the plumes does not depend on their site. We estimated the convecting velocity under the case of
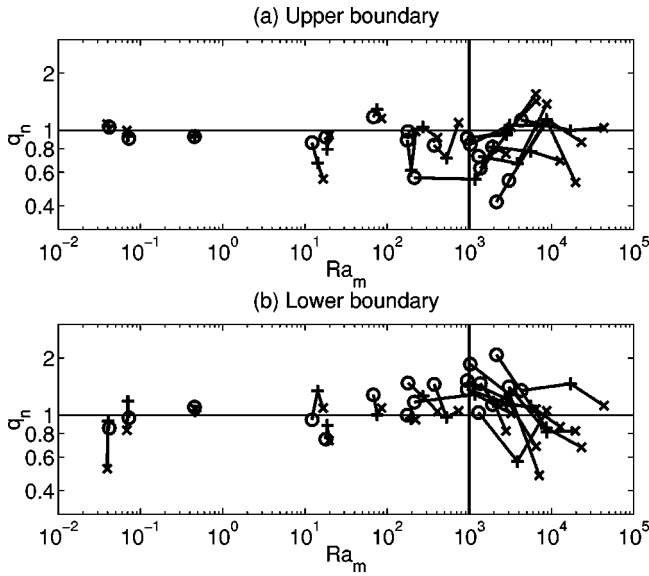
FIG. 11. A lateral variation of the normalized heat flux, Eq. (10), at the upper and lower boundaries as a function of a modified Rayleigh number, Ra_m, Eq. (17). When the Ra_m exceeds $Ra_c \sim 10^3$, the migration of convection cells occurs. When the upper boundary is leveled, we estimate $q_n \sim 1$. $\bigcirc$, $+$, and $\times$ show the measurements at $x/\cos(\theta)=106$, 246, and 367 mm, respectively, at the midwidth of the tank. Measurements from the same experiment are connected by a solid line. A positive gradient for the upper boundary indicates that the heat flux becomes larger (smaller) at the site where the convection layer is thick (thin), and vice versa for the lower boundary. These measurements were made at $Ra_c < Ra_l(x) < 10^7$.

Fig. 3 following Eq. (9), which is $v_{st} \sim 1.4 \times 10^{-3}$ m/s and is not a function of the local height. On the other hand, the measured migrating velocities of the plumes are in the range of $0.4 \times 10^{-3} - 1.5 \times 10^{-3}$ m/s, showing approximate agreement. This suggests that the velocity of the horizontal migrations of plumes depends on the convecting velocity under the region where plumes dominate.

Which scaling law is used to estimate the migrating velocity depends on whether the convection cells appear in the convection pattern.

C. Horizontal heat transfer

In Fig. 8, we showed that the heat transfer is also modified by the inclined upper boundary. We verify the regime in which the horizontal heat transfer becomes significant as follows.

We introduce the modified Rayleigh number Ra_m, which indicates that the migration of the convection cells appears. Arranging Eq. (15) for Ra_c yields an alternative form of the criterion for the migration of convection cells resulting from the tilted upper boundary,

$$Ra_c < [2a\sin(\theta)]^3 Ra_l(x). \tag{17}$$

This relation shows that if $Ra_m = [2a \sin(\theta)]^3 Ra_l(x)$ exceeds Ra_c, the migration of the convection cells occurs.

We now discuss how q_n is modified when the upper boundary is inclined. Figure 11 summarizes how q_n changes
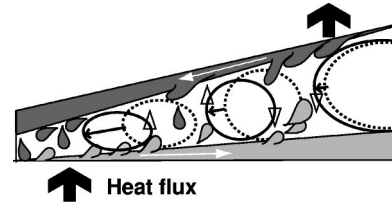

FIG. 12. A schematic diagram of the convection pattern showing how the heat flux is modified by the inclined upper boundary. The leftward migration of the cells is indicated by the arrows.

with Ra_m at regions of different thicknesses. We measured the temperature profiles for each experiment and calculated the heat flux from their gradient. When Ra_m is smaller than Ra_c, Fig. 11 indicates $q_n \sim 1$. However, when Ra_m exceeds Ra_c, Fig. 11 shows that the lateral variation of q_n increases with Ra_m. This shows that the heat flux at the upper boundary becomes larger (smaller) at the site where the convection layer is thick (thin), and vice versa at the lower boundary. The inclined upper boundary generates a lateral variation of the heat flux with a wavelength greater than the width of each cell. Figure 11 also shows that the regime of large-scale heterogeneity in the heat flux corresponds to the regime where the migration of convection cells occurs. We can interpret this result to be a consequence of the lateral transfer of heat and momentum by the plumes, as observed in Fig. 2. We note that the region where maximum heat enters at the lower boundary is the region where minimum heat comes out from the upper boundary. The amplitude of the heat flux heterogeneity increases with the local Rayleigh number and θ.

V. CONCLUSIONS

We have carried out a systematic study of convection under the inclined upper boundary. The convection pattern, temperature fluctuation, and heat transfer are measured with varying the local Rayleigh numbers in the range of $10^3 < Ra_l < 3 \times 10^8$.

The results are schematically shown in Fig. 12. From visual observation, we found a few new convection patterns: at a low Rayleigh number, the simultaneous appearance of migrating convection cells and plumes; at a high Rayleigh number, a large-scale flow originating from the inclined upper boundary. The temperature fluctuations in the regime of the new convection pattern are similar to those of the leveled upper boundary at a Rayleigh number larger than the highest local Rayleigh number of the inclined case. The vertical measurements of the temperature profile show that there is a horizontal heat flux anomaly. The horizontal length scale of the heat flux anomaly exceeds the horizontal scale of each convection cell. This result suggests that the migrating convection cells and plumes transfer the heat horizontally. As a result, the horizontal variation of the vertical heat flux is modified, forming a maximum at the thinnest region in the lower boundary and a maximum at the thickest region in the upper boundary. There is a critical angle that causes the lateral migration of the convection cells. We proposed a model

that explains the critical angle and the time scale of the migration of cells.

APPENDIX A: MEAN TEMPERATURE

The viscosity of glycerol used in our experiments has a temperature dependence, and this causes an asymmetry in the vertical temperature profile. We can estimate the asymmetry of the temperature profile by a simple scaling. The heat flux should be the same between the upper and lower boundaries,

$$\frac{\Delta T_t}{\delta_{th_t}} = \frac{\Delta T_b}{\delta_{th_b}}, \tag{A1}$$

where suffix t and b mean the top and bottom boundaries, respectively. The local Rayleigh number of the upper and lower boundaries should be critical,

$$\mathrm{Ra}_c = \frac{\alpha g \rho \Delta T_t \delta_{th_t}^3}{\eta_t \kappa} = \frac{\alpha g \rho \Delta T_b \delta_{th_b}^3}{\eta_b \kappa}. \tag{A2}$$

From Eqs. (A1) and (A2),

$$\frac{\Delta T_t}{\Delta T_b} = \left(\frac{\eta_t}{\eta_b} \right)^{1/4}. \tag{A3}$$

In our experiments, the maximum viscosity variation in a single experiment has a factor of 2.5, which causes $\Delta T_t \sim 0.56$. Our experimental measurements are consistent with this estimation.

[1] B. Castaing *et al.*, J. Fluid Mech. **204**, 1 (1989).

[2] E. D. Siggia, Annu. Rev. Fluid Mech. **26**, 137 (1994).

[3] K. Fujimura and R. E. Kelly, J. Fluid Mech. **246**, 545 (1993).

[4] K. E. Daniels, B. B. Plapp, and E. Bodenschatz, Phys. Rev. Lett. **84**, 5320 (2000).

[5] F. H. Busse and R. M. Clever, Phys. Fluids **12**, 2137 (2000).

[6] Y.-B. Du and P. Tong, Phys. Rev. Lett. **81**, 987 (1998).

[7] Y. Shen, P. Tong, and K.-Q. Xia, Phys. Rev. Lett. **76**, 908 (1996).

[8] Y.-B. Du and P. Tong, J. Fluid Mech. **407**, 57 (2000).

[9] Y.-B. Du and P. Tong, Phys. Rev. E **63**, 046303 (2001).

[10] P. Jeschke and H. Beer, J. Fluid Mech. **432**, 313 (2001).

[11] R. Krishnamurti, J. Fluid Mech. **60**, 285 (1973).

[12] R. Krishnamurti and L. N. Howard, Proc. Natl. Acad. Sci. U.S.A. **78**, 1981 (1981).

[13] M. Manga and D. Weeraratne, Phys. Fluids **11**, 2969 (1999).

[14] K. C. Stengel, D. S. Oliver, and J. R. Booker, J. Fluid Mech. **120**, 411 (1982).

[15] F. M. Richter, H. C. Nataf, and S. F. Daly, J. Fluid Mech. **129**, 173 (1983).

[16] X.-Z. Wu, L. Kadanoff, A. Libchaber, and M. Sano, Phys. Rev. Lett. **64**, 2140 (1990).

[17] A. Belmonte and A. Libchaber, Phys. Rev. E **53**, 4893 (1996).

[18] G. Zocchi, E. Moses, and A. Libchaber, Physica A **166**, 387 (1990).

[19] S.-Q. Zhou and K.-Q. Xia, Phys. Rev. Lett. **87**, 064501 (2001).

[20] A. Belmonte, A. Tilgner, and A. Libchaber, Phys. Rev. E **50**, 269 (1994).

[21] T. Segawa, A. Naert, and M. Sano, Phys. Rev. E **57**, 557 (1998).